Supplementary Figure 1

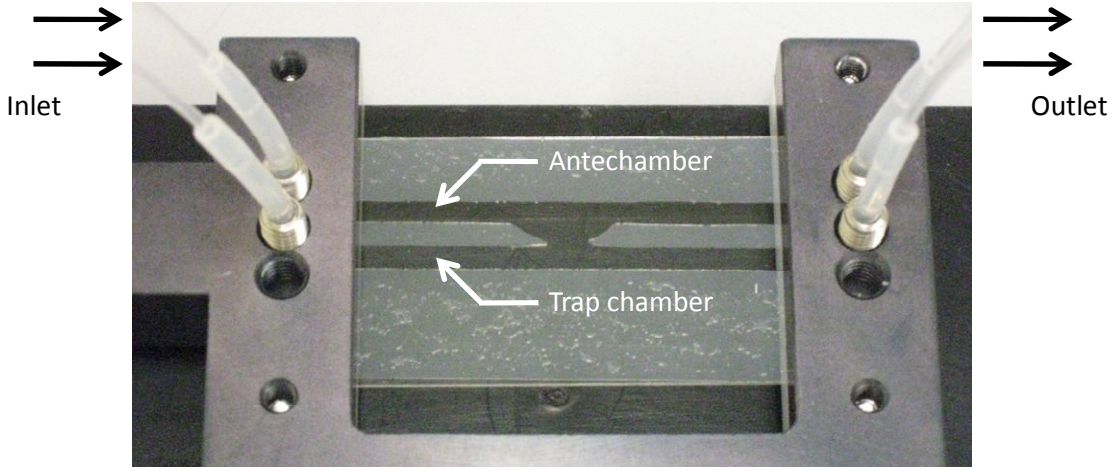

Supplementary Figure 1 | Microfluidic chamber. The antechamber holds trapping medium containing cells. After a cell is trapped, it is moved to the trap chamber, which contains trapping medium but no additional cells. Channel cross-section dimensions are 100 μm x 4000 μm.

Supplementary Figure 2

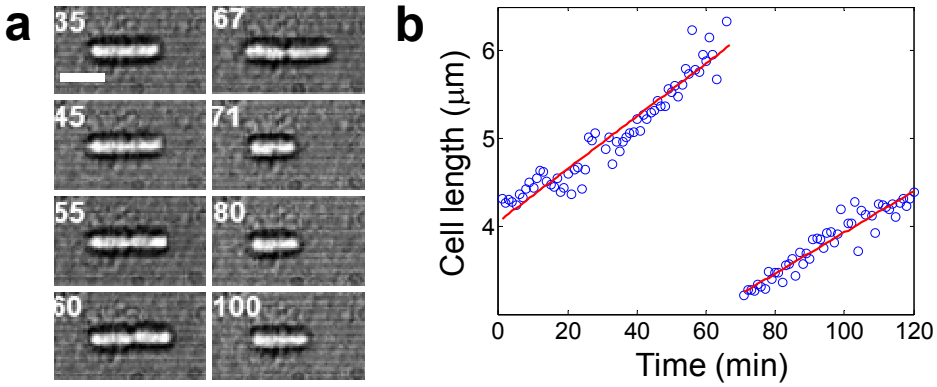

Supplementary Figure 2 | Optically trapped cell grows and divides. (**a**) Brightfield images showing a continuously trapped *E. coli* cell. The cell divides ~70 minutes into observation. Following division, growth of the trapped daughter cell continues. Numbers are in minutes. Scale bar: 2 μm**.** (**b**) Length of the cell in panel **a** measured from brightfield images taken at 1-minute intervals. Red lines are linear fits.

Supplementary Figure 3

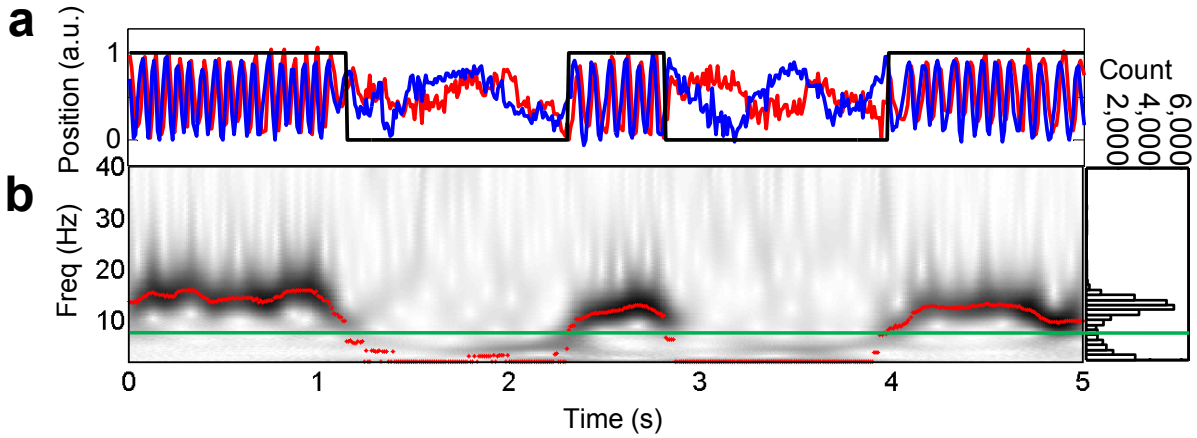

Supplementary Figure 3 | Run-tumble analysis of optical trap data. (**a**) Swimming signal in *y* (red) and *z* (blue) directions from an optically trapped cell, and the binary signal (black) indicating regions of runs (1) and tumbles (0). (**b**) Continuous wavelet transform of the *y* signal in the frequency range 2 – 40 Hz. Red dots indicate the peak frequency component at each time point. Shown on the right is the histogram of peak frequencies from the entire time trace. The frequency value at the local minimum of the histogram is chosen as the threshold (green line), which is used to distinguish runs from tumbles.

Supplementary Figure 4

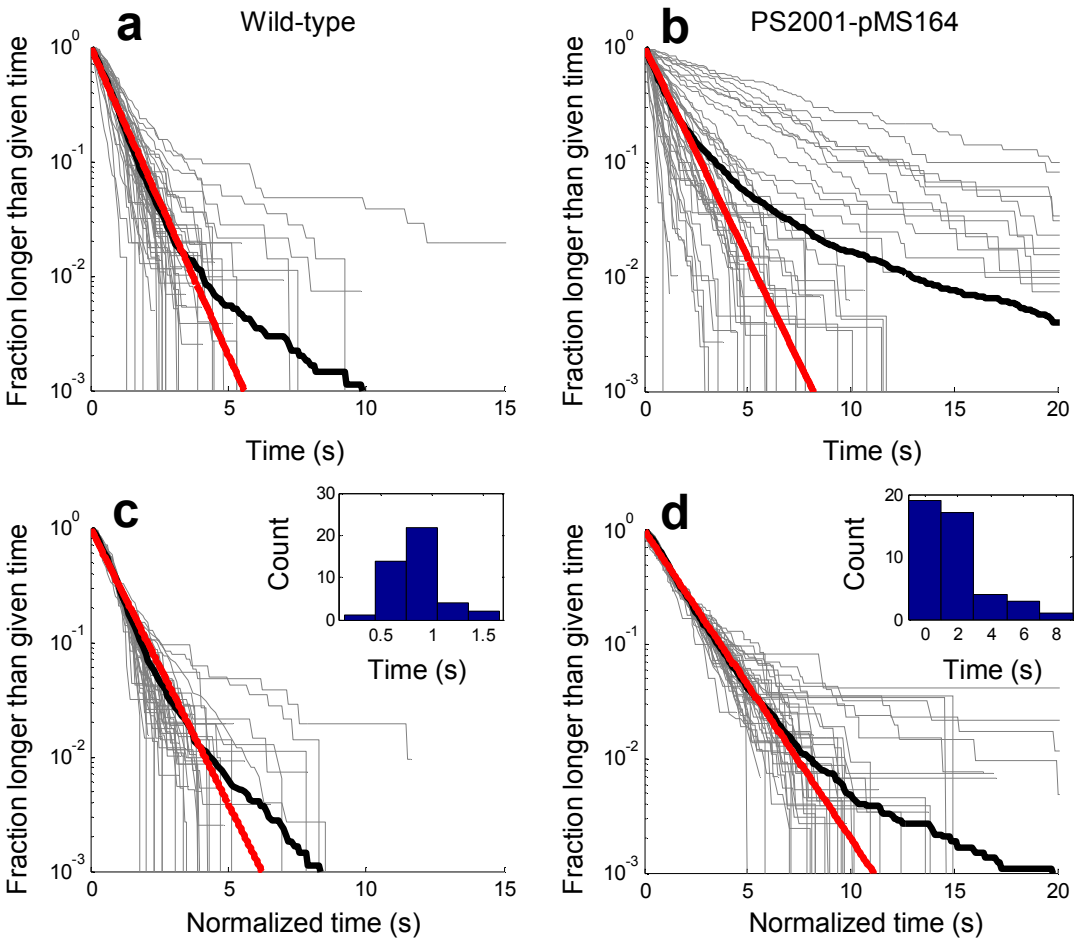

Supplementary Figure 4 | Distributions of tumble duration as detected in the optical trap assay. (**a**) Wild-type cell. Each gray line shows the fraction of tumbles that are longer than a given time. Thick black line is from the population ensemble, comprised of 5,438 tumbles observed from 43 wild-type cells. The red line is an exponential fit to the first decade of the ensemble distribution. (**b**) Same as **a,** for the inducible-bias strain PS2001-pMS164. (**c**) Same as **a**, except that individual tumble duration distributions were scaled so that the mean tumble duration equals the ensemble mean. This scaling procedure collapses data by effectively removing individual variability, thus revealing the underlying universal behavior in the population ensemble. (Inset) Histogram of mean tumble durations used in scaling. (**d**) Same as **c**, for the inducible-bias mutant.

Supplementary Figure 5

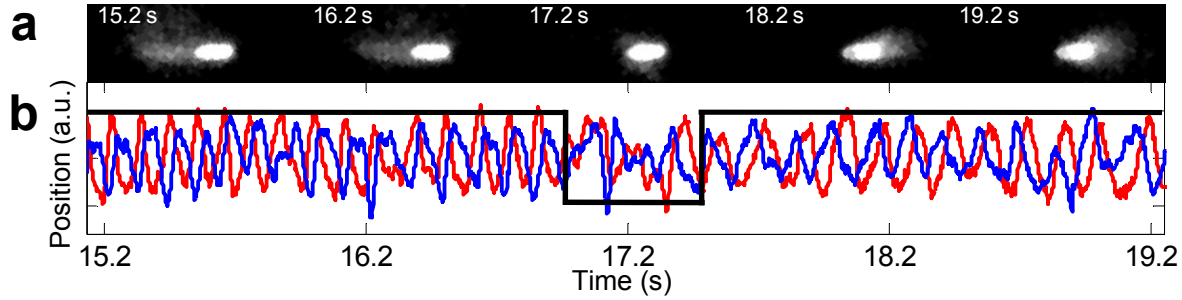

Supplementary Figure 5 | Optically trapped cell undergoing reversal of swimming direction. (**a**) Fluorescence images of a trapped cell. The first two frames (15.2 s, 16.2 s) show the flagellar bundle formed to the left. The third frame (17.2 s) shows the cell tumbling, and the last two frames (18.2 s, 19.2 s) show the flagellar bundle reformed to the right. Each frame was obtained by averaging three successive images collected at a rate of 10 Hz, with the marked time point in the middle. (**b**) Optical trap signal that was recorded simultaneously with the fluorescence images. Signals in *y* (red) and *z* (blue) directions show a reversal of the relative phases, consistent with the reversal of swimming direction evident in the video frames.

Supplementary Figure 6

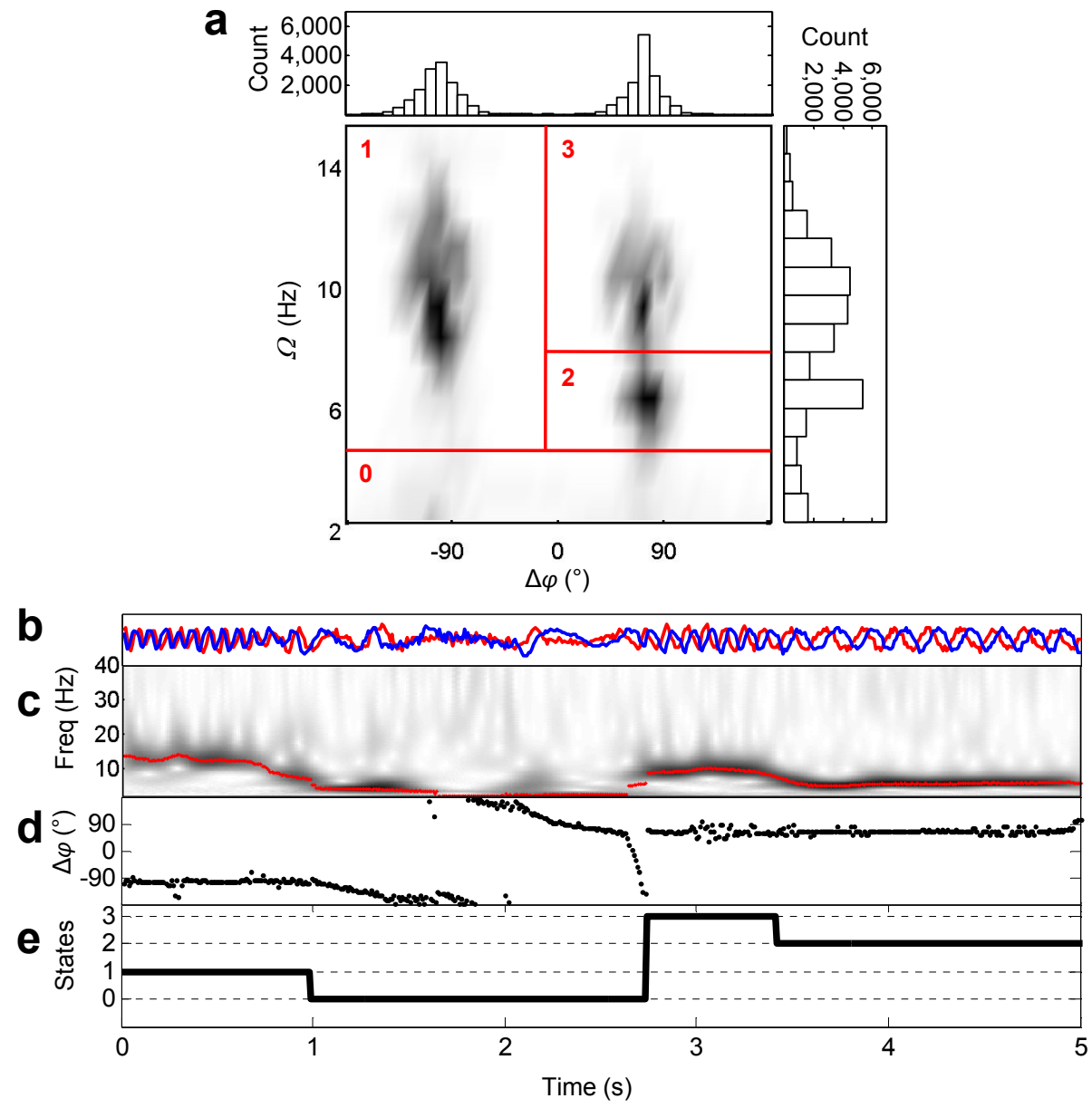

Supplementary Figure 6 | Analysis of optical trap data for multi-state swimming behavior. (**a**) 2-D histogram of body roll frequency (Ω) and phase difference between swimming signals in *y* and *z* directions ($\Delta\varphi$). Red lines divide the histogram into regions of different swimming states (0-3) defined by appropriate ranges of Ω and $\Delta\varphi$. (**b**) A segment of swimming signals in *y* (red) and *z* (blue) directions, taken from the data shown in **a**. (**c**) Continuous wavelet transform of the *y* signal in the frequency range 2-40 Hz. Peak frequency component at each time point is marked by a red dot. (**d**) Phase difference obtained from the phases corresponding to the peak frequency components in *y* and *z* directions. (**e**) Assignment into different states according to Ω and $\Delta\varphi$ values at each time point.

Supplementary Figure 7

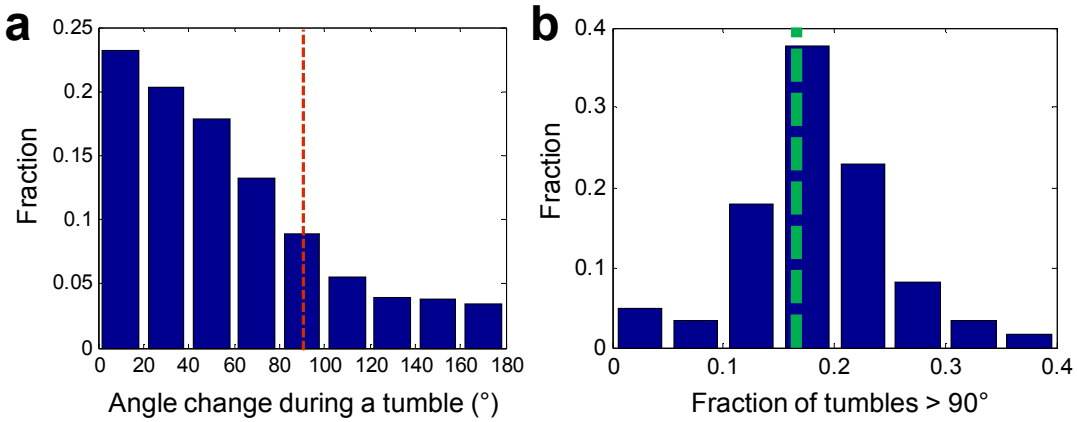

Supplementary Figure 7 | Detection of swimming direction reversal in the 2-D swimming assay. (**a**) Distribution of the angle changes (change in swimming direction) caused by tumbles, as detected in a 2-D swimming movie. Changes greater than 90° (marked by the red dashed line) are assumed to correspond to direction reversals of the 2-D swimming cells. (**b**) Histogram of the fraction of tumbles that result in direction reversals as defined above, from the entire data set of 2-D swimming movies of the wild-type strain. For comparison, the average fraction of tumbles that result in direction reversal from 42 trapped cells is denoted by the green dashed line.

Supplementary Table 1: Strains and plasmid used.

Strain	Genotype	Comments	Source
RP437	*(F- thi thr leu his met eda rpsL)*	Wild type for chemotaxis	Parkinson and Houts (1982)[1] Rao lab stocks
CR20	RP437 (*cheY::FRT*)	"runner" mutant	This study
CR33	RP437 (*cheZ::cm*)	"tumbler" mutant	This study
PS2001	*ΔcheBcheYcheZ*	Contains the plasmid pMS164 for adjustable tumble bias	Alon et al. (1998)[3] Gift of Philippe Cluzel (Harvard University)
Plasmid			
pMS164	Low copy, *cheYD13K* under *lac* promoter, Cm^R	Expresses constitutively active mutant version of CheY	Alon et.al. (1998)[3] Gift of Philippe Cluzel

Supplementary Table 2: Comparison of trapping media.

Buffer	Contents	Body roll rate Ω (Hz)	Flagella rotation rate ω (Hz)	Tumble frequency (Hz)
Trapping medium	TB, 100 mM Tris, 2% (wt/vol) glucose, oxygen scavenging system	11.4 ± 0.5 (mean±s.e.m., *n* = 43)	86.1 ± 1.7	0.22 ± 0.02
High ionic-strength motility buffer	70 mM NaCl, 100 mM Tris, 2% (wt/vol) glucose, oxygen scavenging system	7.0 ± 1.1 (mean ± s.e.m., *n* = 8)	80.5 ± 3.8	0.23 ± 0.03
Low ionic-strength motility buffer	70 mM NaCl, 10 mM Tris, 2% (wt/vol) glucose, oxygen scavenging system	9.1 ± 1.1 (mean ± s.e.m., *n* = 7)	72.9 ± 1.7	0.25 ± 0.02

Supplementary Table 3: Primer sequences.

Name	Sequence
Y_F	GTG CCG GAC AGG CGA TAC GTA TTT AAA TCA GGA GTG TGA AGT GTA GGC TGG AGC TGC TTC
Y_R	GTC AGC AGG TTT GAT TGA TGG TTG CAT CAT AGT CGC ATC CCA TAT GAA TAT CCT CCT TAG
Z_F	AAC AAA ATC TTT GAG AAA CTG GGC ATG TGA GGA TGC GAC TGT GTA GGC TGG AGC TGC TTC
Z_R	AAC AAA ATC TTT GAG AAA CTG GGC ATG TGA GGA TGC GAC TGT GTA GGC TGG AGC TGC TTC

Supplementary Note 1: Limitations of current assays for cell motility.

The two standard methods for assaying bacterial swimming and chemotaxis suffer important limitations. The free swimming assay typically yields data that are limited to relatively short time periods[1-3]. When three-dimensional motion is followed, sophisticated custom-made optics allows tracking the cells up to ~30 seconds[1,2], not enough to characterize such features as long-term fluctuations in inter-event times[4] and chemotactic adaptation times[5]. When bacterial swimming is limited to two dimensions (2D), longer trajectories can be acquired (several minutes[6]). Still, data acquisition is limited by multiple factors such as rotational Brownian motion (which limits the ability to classify "runs" and "tumbles"[7]) and interaction with the surface[8]. Last, the fact that the cells actually swim—thereby changing their position—makes it impossible to impose an arbitrary stimulus (e.g. a constant gradient of attractant) on each cell throughout the experiment.

As for the tethered-cell assay, one of the main limitations is that it probes the activity of a single motor, rather than the physiologically relevant whole-cell swimming phenotype. A typical *E. coli* cell has 3-5 flagella[9], each driven by its own motor. These motors are subject to the competing effects of common control via diffusive fields in the cell on one hand[10,11], countered by the stochasticity of the individual motor on the other[12,13]. The resulting cell's run/tumble behavior is a complex outcome of the multi-motor state. Tethered-cell assays are also notorious for their low efficiency; typically multiple tethered cells are tracked under the microscope, with only a few exhibiting the "proper" phenotype[14].

Supplementary Note 2: On the relation between trap oscillatory frequencies and cell motility.

The flagellar rotation rate ω and body roll frequency Ω shed light on the swimming mechanics of the cell. Loosely speaking, ω determines the propulsive force and torque generated by the flagellar bundle (both also depend on parameters such as the number, spatial arrangement, and geometry of the flagella: length, helical pitch, etc.[15]). The swimming speed v and body roll Ω are determined by the balance between the propulsive force and torque and the viscous linear and rotational drag of the cell body, respectively[15]. Importantly, it follows that any variation in rate or conformational state of the flagellar bundle will likely be manifested in changes in both v and Ω.

Supplementary Note 3: Difference in tumble duration between trapped and free-swimming cells.

One difference in behavior between trapped cells and free-swimming cells is that the average tumble duration measured by our method, 0.85 ± 0.03 s (mean ± s.e.m., *n* = 43), is longer than that previously reported, 0.1 - 0.2 s[2,3,16]. One possible reason for such difference is our tumble detection algorithm, which artificially imposes a lower limit on the allowed tumble duration (**Online Methods**). More likely is that this discrepancy reflects a difference in definition of a tumble interval between the assays. In cell tracking assays, a tumble is defined as the interval between the end of one run and the start of another[2]. In the trap assay, it is defined as a period of erratic motion. Since the flagellar bundle is not fully formed as the cell resumes a run[17], it is likely that erratic rotational motion persists at the start of a run; steady body roll resumes only once the full flagellar bundle is formed. Although trapped, swimming cells may exhibit subtle differences in mechanics, the important decision-making process of running or tumbling does not appear to be affected, as reflected by the control experiments described in the main text and by the reasonable match in average run durations measured by our trap assay and by traditional methods[6].

Supplementary Note 4: On the possible role of reversals.

It is well established that the distribution of turn-angles after a tumble is biased toward the initial swimming direction[9], and reversals thus may be utilized by cells to randomize their orientation more efficiently. To corroborate this interpretation, we performed cell tracking experiments in a 2-D chamber[16] with the same strain, and monitored the change in orientation of individual bacteria after a tumble. As shown in **Supplementary Figure 7**, the distribution of angular change is biased toward the initial orientation, as expected, but also indicates events at large angles (>90°). The probability of reorientation by large angles is 18.1 ± 0.1% (mean ± s.e.m., *n* = 61), consistent with previous studies (~25%[2]) and in good agreement with the 1 in 6 likelihood of reversing after a tumble observed in the trap. The reversal probability represents the likelihood of reforming the flagellar bundle on the opposite end of the cell after a tumble. The fact that this probability is less than 50% is probably due to the maintenance of a partial bundle during most tumbles[9]. Changes in velocity upon reversals likely reflect the fact that bundles formed on opposite ends of the cell may have different spatial arrangements and may thus couple different propulsive forces and torques to the cell body despite identical flagellar rotation rates (see **Supplementary Note 1**).

Supplementary Note 5: Changes in swimming speed.

The observations of changes in body roll rate Ω with no accompanying reversal in swimming direction or corresponding changes in flagellar rotation frequency ω may again reflect changes in propulsive force and torque coupled to the cell body from the flagellar bundle (see **Supplementary Note 1**). In contrast to the case of reversals, however, the spatial orientation of the flagella is unlikely to change in these events, and we speculate that changes in the number of flagella involved in the bundle may be the ultimate cause. This mechanism may explain why speed changes only occasionally follow tumbles, as counter-rotation of one flagellum is necessary to trigger a tumbling event, but does not guarantee a tumble[9]. Improved fluorescence imaging should provide a definitive answer to this question.

Supplementary Note 6: Bias of cell swimming.

Bias in swimming direction can be quantified in terms of the number of runs $r_{\pm}$ in the $\pm x$ direction for each individual cell ($\pm x$ corresponds to $\Delta\phi = \pm 90°$ in the histograms). While the "preference" in direction, defined as $(r_+ - r_-)/(r_+ + r_-)$, has a negligibly small value of 0.008 ± 0.061 averaged over the cell population (49.6 ± 4.3% of all runs are along the $+x$ direction, compared to 50.4 ± 4.3% along $-x$), the "bias" in individual cells, defined as $|r_+ - r_-|/(r_+ + r_-)$, has a mean of 0.47 ± 0.04 (all values are mean ± s.e.m., n = 42). This value represents a significant deviation from the expected random statistical variations due to the finite sample size (a total of 5404 runs observed). Although this bias is larger than that reported in a previous study[6], it may similarly reflect asymmetries in the spatial arrangements of flagella at the cell ends, a question that could be addressed in the future with improved fluorescence imaging.

Supplementary Note 7: Future experimental directions.

Future enhancements should further our advance towards the development of an integrated device for the quantitative phenotyping of bacterial swimming, as well as other physiological parameters, while the cells are subjected to precise spatiotemporal stimuli. By immobilizing the cell in the optical traps, our technique gives us the ability to precisely displace an individual bacterium within a well-controlled microfluidic environment. For example, parallel laminar streams can be used to establish a stepwise

concentration profile in a flow chamber[18]. Alternately, a constant spatial gradient can be created by shunting two reservoirs containing different media to opposite ends of the chamber[19]. This will allow us to create any arbitrary spatiotemporal stimulus pattern and measure cellular response, in particular the run-tumble statistics of a cell moving up or down a chemoeffector gradient and chemotactic adaptation at the single-cell level. Enhancement of the fluorescence readout capability of the instrument will be necessary to enable the measurement of additional cellular parameters during free swimming and chemotaxis: the dynamics of individual flagella, expression levels of key genes, and localization of signal transduction components. Incorporating high-resolution fluorescence imaging into the apparatus is a difficult technical challenge. The fast dynamics of individual flagella (~100 Hz) requires high-speed video acquisition or stroboscopic illumination[9] to resolve. More importantly, optical traps can induce rapid photobleaching of dye molecules[20]. However, as shown by Brau et al.[20], rapid (50 kHz) interlacing of trapping and fluorescence excitation light sources to prevent simultaneous exposure mitigates these effects significantly.

Supplementary references

1. D. A. Brown and H. C. Berg, *Proc Natl Acad Sci U S A* **71** (4), 1388 (1974).
2. H. C. Berg and D. A. Brown, *Nature* **239** (5374), 500 (1972).
3. J. F. Staropoli and U. Alon, *Biophysical Journal* **78** (1), 513 (2000).
4. E. Korobkova, T. Emonet, J. M. G. Vilar et al., *Nature* **428** (6982), 574 (2004).
5. U. Alon, M. G. Surette, N. Barkai et al., *Nature* **397** (6715), 168 (1999).
6. H. C. Berg and L. Turner, *Proceedings of the National Academy of Sciences of the United States of America* **92** (2), 477 (1995).
7. H. C. Berg and E. M. Purcell, *Biophys J* **20** (2), 193 (1977).
8. M. A. Vigeant and R. M. Ford, *Appl Environ Microbiol* **63** (9), 3474 (1997).
9. L. Turner, W. S. Ryu, and H. C. Berg, *Journal of Bacteriology* **182** (10), 2793 (2000).
10. Howard C. Berg, *E. coli in motion*. (Springer, New York, 2004).
11. Uri Alon, *An introduction to systems biology : design principles of biological circuits*. (Chapman & Hall/CRC, Boca Raton, FL, 2007).
12. A. Ishihara, J. E. Segall, S. M. Block et al., *Journal of Bacteriology* **155** (1), 228 (1983).
13. R. M. Macnab and D. P. Han, *Cell* **32** (1), 109 (1983).
14. H. Mao, P. S. Cremer, and M. D. Manson, *Proc Natl Acad Sci U S A* **100** (9), 5449 (2003).
15. S. Chattopadhyay, R. Moldovan, C. Yeung et al., *Proceedings of the National Academy of Sciences of the United States of America* **103** (37), 13712 (2006).
16. U. Alon, L. Camarena, M. G. Surette et al., *EMBO J* **17** (15), 4238 (1998).
17. N. C. Darnton, L. Turner, S. Rojevsky et al., *Journal of Bacteriology* **189** (5), 1756 (2007).
18. L. R. Brewer and P. R. Bianco, *Nat Methods* **5** (6), 517 (2008).
19. J. Diao, L. Young, S. Kim et al., *Lab Chip* **6** (3), 381 (2006).
20. R. R. Brau, P. B. Tarsa, J. M. Ferrer et al., *Biophys J* **91** (3), 1069 (2006).